scientific reports

OPEN

Multi-level characteristics of TiO$_x$ transparent non-volatile resistive switching device by embedding SiO$_2$ nanoparticles

Sera Kwon, Min-Jung Kim & Kwun-Bum Chung[✉]

TiO$_x$-based resistive switching devices have recently attracted attention as a promising candidate for next-generation non-volatile memory devices. A number of studies have attempted to increase the structural density of resistive switching devices. The fabrication of a multi-level switching device is a feasible method for increasing the density of the memory cell. Herein, we attempt to obtain a non-volatile multi-level switching memory device that is highly transparent by embedding SiO$_2$ nanoparticles (NPs) into the TiO$_x$ matrix (TiO$_x$@SiO$_2$ NPs). The fully transparent resistive switching device is fabricated with an ITO/TiO$_x$@SiO$_2$ NPs/ITO structure on glass substrate, and it shows transmittance over 95% in the visible range. The TiO$_x$@SiO$_2$ NPs device shows outstanding switching characteristics, such as a high on/off ratio, long retention time, good endurance, and distinguishable multi-level switching. To understand multi-level switching characteristics by adjusting the set voltages, we analyze the switching mechanism in each resistive state. This method represents a promising approach for high-performance non-volatile multi-level memory applications.

The resistive switching device has attracted attention as a promising candidate for next-generation non-volatile memory devices, as it is can be used to achieves low power consumption, good storage capability, high-speed operation, and stable switching properties[1–4]. Many kinds of inorganic transitional metal oxide materials have been proposed for the active layer, including TiO$_2$, Ta$_2$O$_5$, HfO$_2$, and NiO[5–8]. Among them, TiO$_2$ has been widely studied due to its fast switching speed, promising performance, intrinsic variety of crystal phases, and the associated richness of its switching dynamics, as well as change of the operating characteristics according to the ambient condition[9–12]. Recently, scaling down the device size and increasing the structural density of the memory array have become highly sought after targets in resistive random access memory (ReRAM) devices. The cross-bar array architecture is a widely accepted method with structural benefits, which is sandwiched by inserting active layer between the parallel bottom electrode (BE) and perpendicular to the top electrode (TE)[13–15]. Another aspect that has received considerable attention is the fabrication of a multi-level switching device, which can store multi-bit data in one cell and can enhance the physical density of the memory device[4,16,17]. In general, a resistive switching device changes electrically between a high resistive state (HRS) and a low resistive state (LRS) through the application of electrical inputs. By contrast, the multi-level switching device has various HRS or LRS; specifically, the multi-level switching characteristics can be generated by either modifying the length of the gap between the conductive filament (CF) and electrode, which is controlled by adjusting the stop voltage during the RESET process, or by controlling the diameter/density of the CF during the LRS process[18–20]. Recent research has indicated that the switching performance of a switching device can be improved by incorporating nanostructures into the matrix of the switching layer. Tsigkourakos et al. has reported the fabrication of a TiO$_{2-x}$-based resistive switching device by embedding Pt nanocrystals, and this device achieved low power operation current and obtained multi-level switching characteristics by controlling the compliance current[21]. Yoon et al. embedded Ru nanodots into TiO$_x$ thin film to achieve resistive switching uniformity among TiO$_2$ memory cells[22]. The embedment of metal nanostructures has attracted substantial attention, as it improves the resistive switching performance by controlling the size and shape. However, metal nanostructure-embedded switching device has a crucial issue for fabrication of transparent switching devices, due to the inherent opaqueness of metal; this means it is unfeasible to use such devices in next-generation memory devices. Transparent memory devices are extremely useful due to their potential applications in the field of transparent electronics. Herein, we

Division of Physics and Semiconductor Science, Dongguk University, Seoul 04620, Republic of Korea. [✉]email: kbchung@dongguk.edu
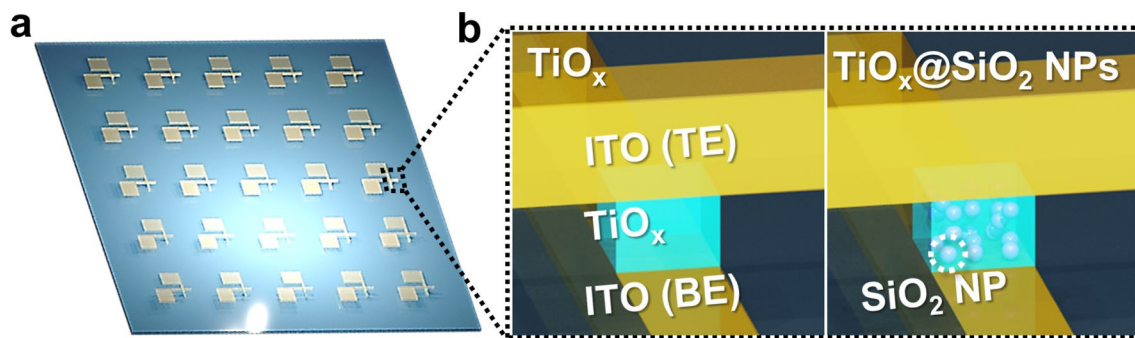
Figure 1. (**a**) Schematic illustration of cross-bar arrays of the TiO$_x$ switching device. (**b**) Enlarged view of the cross-section region of the switching device unit cell.

attempt to achieve fully transparent non-volatile memory devices, as well as multi-level switching characteristics, by using SiO$_2$ nanoparticles (NPs).

In this study, we prepared a multi-level switching device with transparent characteristics by embedding SiO$_2$ NPs into the TiO$_x$ matrix (structure with ITO/SiO$_2$ NPs-embedded TiO$_x$/ITO) on glass substrate using a solution process, as shown in Fig. 1. The SiO$_2$ NPs-embedded TiO$_x$ device showed high transmittance as well as outstanding electrical performance, including a large on/off current ratio, long retention time, good endurance, and multi-switching characteristics.

Results and discussion

Figure 2a,b show the surface morphologies of the TiO$_x$ and TiO$_x$@SiO$_2$ NPs films, which were obtained using atomic force microscopy (AFM) measurement. It can clearly be seen that the nano-particles with a sphere shape are well embedded into the TiO$_x$ matrix. In addition, the root-mean-square (RMS) roughness values for TiO$_x$ and TiO$_x$@SiO$_2$ NPs are changed from 0.42 to 2.95 nm, respectively. Further, the average height of SiO$_2$ NPs is approximately 20.61 nm, as shown in Fig. 2c. Moreover, TEM measurement was conducted to examine the cross-sectional structures of the TiO$_x$ and TiO$_x$@SiO$_2$ NPs switching devices. As shown in Fig. 2d,e, the TEM image of the TiO$_x$ device clearly shows stacking of ITO/TiO$_x$/ITO. On the other hand, the brighter areas with a spherical shape that are well distributed in the region of the TiO$_x$@SiO$_2$ NPs layer are estimated to be SiO$_2$ NPs. For a detailed analysis of the bright areas in the TiO$_x$@SiO$_2$ NPs layer, high-angle annular dark-field scanning TEM (HAADF-STEM) was taken across the TiO$_x$ and TiO$_x$@SiO$_2$ NPs, as shown in Fig. 2f,j. According to HAADF-STEM, the heavy element shows bright contrast, while the light element shows dark contrast[23]. In the HAADF-STEM image of TiOx@SiO$_2$ NPs, the darker region that exists in the shape of a sphere in the TiO$_x$ matrix corresponds to SiO$_2$ NPs. To investigate the chemical species, EDS spectra are taken. In Fig. 2g–i, only Ti and O elements are detected in the case of the TiOx device, whereas the TiO$_x$@SiO$_2$ NPs device is composed of Ti, O, and Si as shown in Fig. 2k–m. Based on the cross-sectional information, the distribution of SiO$_2$ NPs in TiO$_x$ is definitively confirmed.

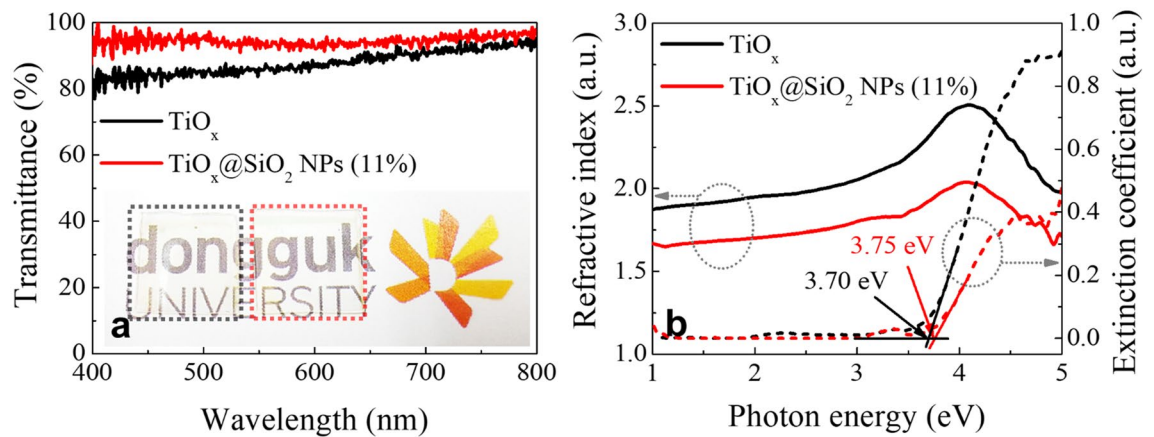Figure 3a shows the transmittances of the ITO/TiO$_x$/ITO device and the ITO/TiO$_x$@SiO$_2$ NPs/ITO structures. As shown in the inset in the Fig. 3a, the two devices are both highly transparent. To compare the optical transmittances values of the TiO$_x$ and TiO$_x$@SiO$_2$ NPs devices, we measured the optical transmittance in the visible range from 400 to 800 nm, and we ultimately obtained respective values of 87 and 95%. It is concluded that the optical transmittance is improved by embedding SiO$_2$ NPs into TiO$_x$. Figure 3b shows the refractive index and extinction coefficient of TiO$_x$ and TiO$_x$@SiO$_2$ NPs, which were obtained using a four-phase model comprising glass substrate, ITO layer, TiO$_x$ layer, and ambient layer[24]. For the TiO$_x$ film, the refractive index was 1.96, which is smaller than that of conventional TiO$_2$ film (which ranges from 2.4 to 2.75 at 550 nm)[25]. As research has shown that the refractive index can be related to the film density, we consider that a decrease in the refractive index for the prepared TiO$_x$ film implies a lower density than that of conventional TiO$_2$ film[26,27]. In the TiO$_x$@SiO$_2$ NPs, the value of the refractive index decreases to 1.72, as it is affected by the embedment of the small refractive index of SiO$_2$ NPs (~ 1.47)[28]. Embedding SiO$_2$ NPs into the TiO$_x$ matrix also leads to a decrease in the extinction coefficient, which represents a decrease in absorption. The optical band gap can be extracted by extrapolating the linear portion of the extinction coefficient. The optical band gap of TiO$_x$ and TiO$_x$@SiO$_2$ NPs is found to be 3.70 and 3.75 eV, respectively. These values are consistent with the TiO$_x$ films made by the solution process, and the TiO$_x$ and TiO$_x$@SiO$_2$ NPs are both completely transparent in the visible region[29].

Figure 4a–e respectively show the Ti 2p, O 1s, and Si 2p core-level spectra of the TiO$_x$ and TiO$_x$@SiO$_2$ NPs films. The XPS analysis was conducted after surface sputtering for 10 s to eliminate the carbon contamination, which was performed by Ar sputtering at 500 W. The survey spectra were measured to acquire accurate compositions of the TiO$_x$ and TiO$_x$@SiO$_2$ NPs films (Fig. S1). In the case of TiO$_x$@SiO$_2$ NPs, the TiO$_x$ matrix consists of 11.5% Si. To elucidate the chemical bonding states, the core-level spectra of Ti 2p, O 1s, and Si 2p were normalized, then deconvoluted into Gaussian peaks. Figure 4a,c show the Ti 2p spectra, wherein the two peaks centered at 459.15 and 453.45 eV can be attributed to Ti 2$p_{1/2}$ and Ti 2$p_{3/2}$, respectively. The separation between these two peaks is calculated to be ~ 5.7 eV, which suggests the existence of Ti^{4+} oxidation states in the TiO$_2$[30]. The shoulder peaks at 458.15 and 452.45 eV can be correlated with the Ti^{3+} oxygen deficient states in TiO$_x$, which originate from the reduction of Ti^{4+} by free electrons donated by oxygen vacancies[29,31]. In the TiO$_x$@SiO$_2$ NPs, the intensity
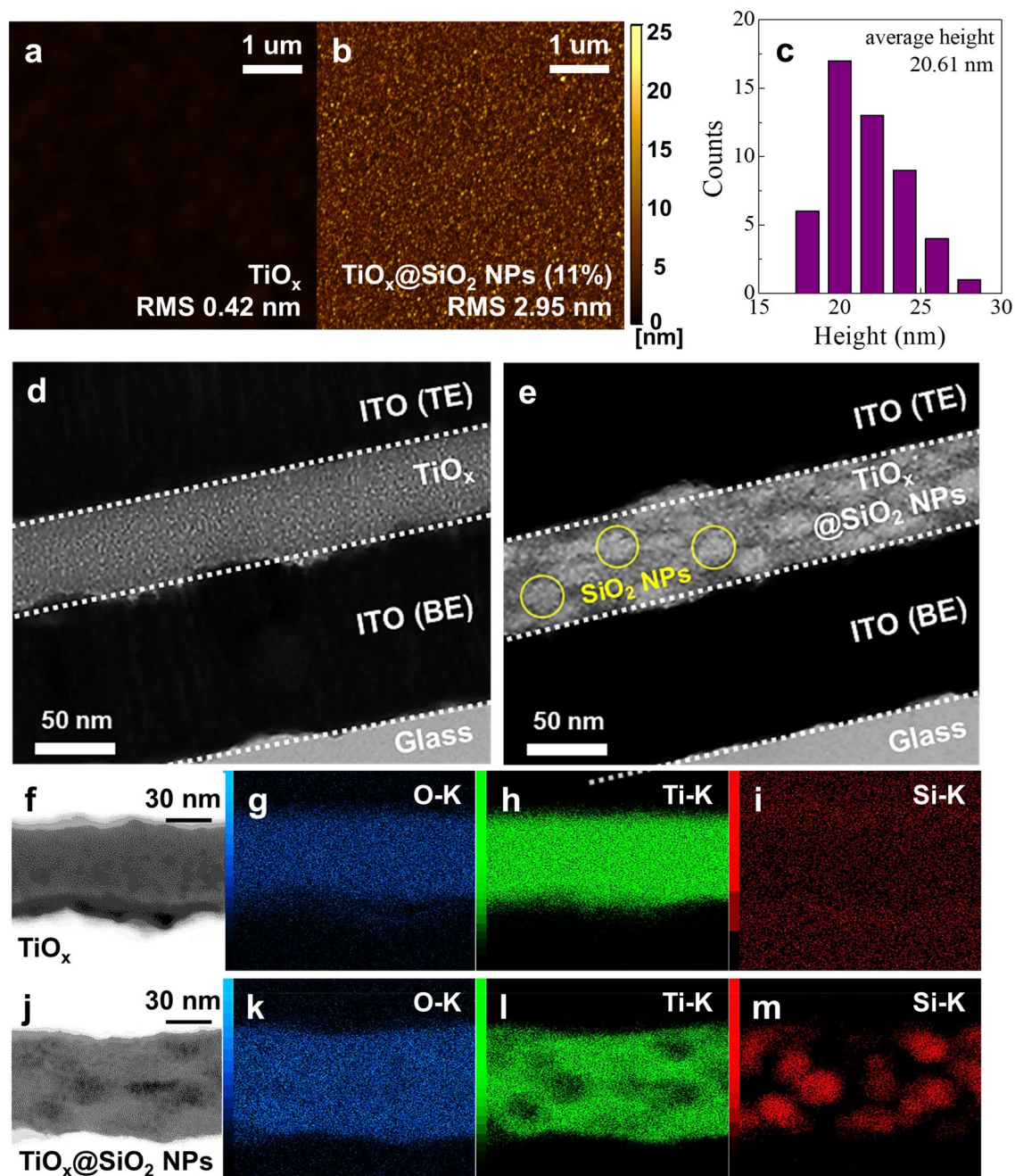
Figure 2. (**a,b**) AFM topographic images, (**c**) average height of SiO_2 NPs, (**d,e**) cross-sectional TEM images, and (**f–i**) HAADF-STEM and EDS spectra of TiO_x and (**j–m**) $TiO_x@SiO_2$ NPs structures.

of the Ti^{3+} peaks slightly increases relative to those of the TiO_x, which is attributed to the $TiO_x@SiO_2$ NPs sample having more oxygen deficient state in the TiO_x matrix. The O 1s peaks are composed of three Gaussian peaks corresponding to the Ti–O bonds at 531 ± 0.2 eV (O1), oxygen deficient states at 532 ± 0.2 eV (O2), and hydroxyl groups at 533 ± 0.2 eV (O3), respectively, as shown in Fig. 4b,d[32]. Upon embedding the SiO_2 NPs into the TiO_x matrix, the O2 peak of the $TiO_x@SiO_2$ NPs drastically increases compared to those of the TiO_x. There is also an increase in the O3 peak, which is associated with an increased number of residual surface hydroxyl groups; however, this is disputable, because the binding energies of the Si–O bonds overlap the hydroxyl groups attributed to O3[33]. In our explanation, the effect of the surface hydroxyl groups is negligible, because the dominating mechanism for the TiO_x-based switching device comes from the oxygen vacancies. Si 2p is composed of regular SiO_2 (Si^{4+}) as well as a substantial amount of oxygen deficient states in SiO_x (Si^{3+}), as shown in Fig. 4e[34]. This indicates that the $TiO_x@SiO_2$ NPs has a higher composition of oxygen vacancies than TiO_x. These results can be attributed to the migration of oxygen ions from the TiO_x matrix into SiO_2 NPs, which is caused by the higher bond dissociation energy of Si–O (799.6 ± 13.4 kJ/mol) than that of Ti–O (666.5 ± 5.6 kJ/mol); therefore, the embedment of SiO_2 NPs is shown to produce the oxygen deficient states in the TiO_x matrix[35]. In the TiO_x-based

Figure 3. (**a**) Optical transmittance and (**b**) optical constants of the TiO_x and $TiO_x@SiO_2$ NPs films. Inset shows the high transparency of the TiO_x (left) and $TiO_x@SiO_2$ NPs (right) switching devices.

ReRAM, defects such as oxygen deficient states play an important role in the switching characteristics, which is strongly related to the migration of oxygen vacancies and the formation/rupture of the conductive path caused by the application of an external electric field[36]. It is also known that the physical size of the conductive filament depends on the concentration of oxygen vacancies. Thus, the size of the conductive filament for the $TiO_x@SiO_2$ NPs is expected to be wider than that of the TiO_x device, and various electrical characteristics, such as multi-level switching, can be expected.

Electrical characteristics. Figure 5a,b show the typical I–V curves under voltage sweeping for the TiO_x and $TiO_x@SiO_2$ NPs switching devices after the electro-forming process (Fig. S2). Initially, the TiO_x-based switching device is in HRS, because of the Schottky barrier at the interface of the electrode/TiO_x. In our device structure with ITO/TiO_x/ITO, the electron transport is limited due to the difference between the work-function of the ITO electrode (~ 4.4 eV) and TiO_x (~ 3.8 eV)[37,38]. As shown in Fig. 5a,b, both devices exhibit bipolar resistive switching characteristics. Regarding the TiO_x device, it switches from HRS to LRS, and the SET process is achieved by sweeping the voltage from 0 to 0.56 V. When sweeping the voltage from 0 to − 0.62 V, the state changes from LRS to HRS, and the RESET process can be obtained. It is known that TiO_2 has the coexistence of bipolar resistive switching characteristics, thus they can be achieved SET/RESET process in both polarity regardless of the voltage polarity of the electro-forming process[39]. For the $TiO_x@SiO_2$ NPs device, it is clearly indicated that the multi-step SET process can be obtained by controlling the voltage. When the positive voltage sweeps from 0 to 1.2 V, the RS transits from the HRS to the lowest LRS, denoted as LRS1. Upon increasing the voltage to 2.2 V, the intermediate LRS (LRS2) can be achieved. And then, further increasing the voltage to 3.3 V, the highest LRS can be obtained, it indexed to LRS3. From sweeping the positive voltage, we obtain multi-level switching characteristics with four storage levels. During the negative voltage sweeps, the RS changes from LRS to HRS. It can be attributed that the SiO_2 NPs are a little more existed at the interfaces of $TiO_x@SiO_2$ NPs/top electrode than that of interfaces of $TiO_x@SiO_2$ NPs/bottom electrode (Fig. S3). When the electrons are injected from top electrode into $TiO_x@SiO_2$ NPs layer, SiO_2 NPs suppress the carrier transport, thus, the switching device maintains the HRS under negative voltage. Consequentially, SiO_2 NPs with high bandgap provides the asymmetric potential barrier for the bipolar resistive switching[40]. Another interesting result is that the current level slightly decreases compared to that of the TiO_x device, meaning that the ratio of HRS/LRS is also improved. This result indicates that the SiO_2 NPs act as an insulating layer. To ensure that the multi-level switching characteristics are due to the embedment of SiO_2 NPs, the switching mechanism was examined as a function of the composition of SiO_2 NPs, and it was found that the multi-level switching characteristics appeared slightly at the low composition (Fig. S4). Based on the I–V analysis, it can be concluded that the embedment of SiO_2 NPs into the TiO_x matrix can significantly improve the resistive switching performance, such as multi-level switching, and obtain a high ratio of HRS/LRS for TiO_x-based switching devices.

To examine the stability of the device, as shown in Fig. 5c,d, the retention was studied by probing the RS changes in the HRS and LRS states for 10^3 s at room temperature, and measurements were performed by separately reading the current at 0.1 V after the SET and RESET processes. The TiO_x device maintained a stable HRS/LRS ratio over 10^2 for 10^3 s. The $TiO_x@SiO_2$ NPs device exhibits four well-defined RSs (HRS, LRS 1, LRS 2, and LRS 3), each of which is observed for 10^3 s. Further, to examine the endurance performance, the RS cycling test was conducted for 10^2 cycles after the SET and RESET processes, as shown in Fig. 5e,f. The two devices both show stable HRS/LRS ratios for 10^2 cycles. Specifically, in the case of the $TiO_x@SiO_2$ NPs, multiple RSs are well defined for 10^2 cycles. The long retention time and high endurance indicate the high reliability and non-volatile nature of the TiO_x-based resistive switching devices.

Switching mechanism. The conduction mechanism of the TiO_x and $TiO_x@SiO_2$ NPs devices can be obtained by analysing the I–V curves. For the TiO_x device, the fitting results for HRS suggest that the charge transport mechanism is in good agreement with a trap-controlled space charge limited conduction (SCLC), as

4
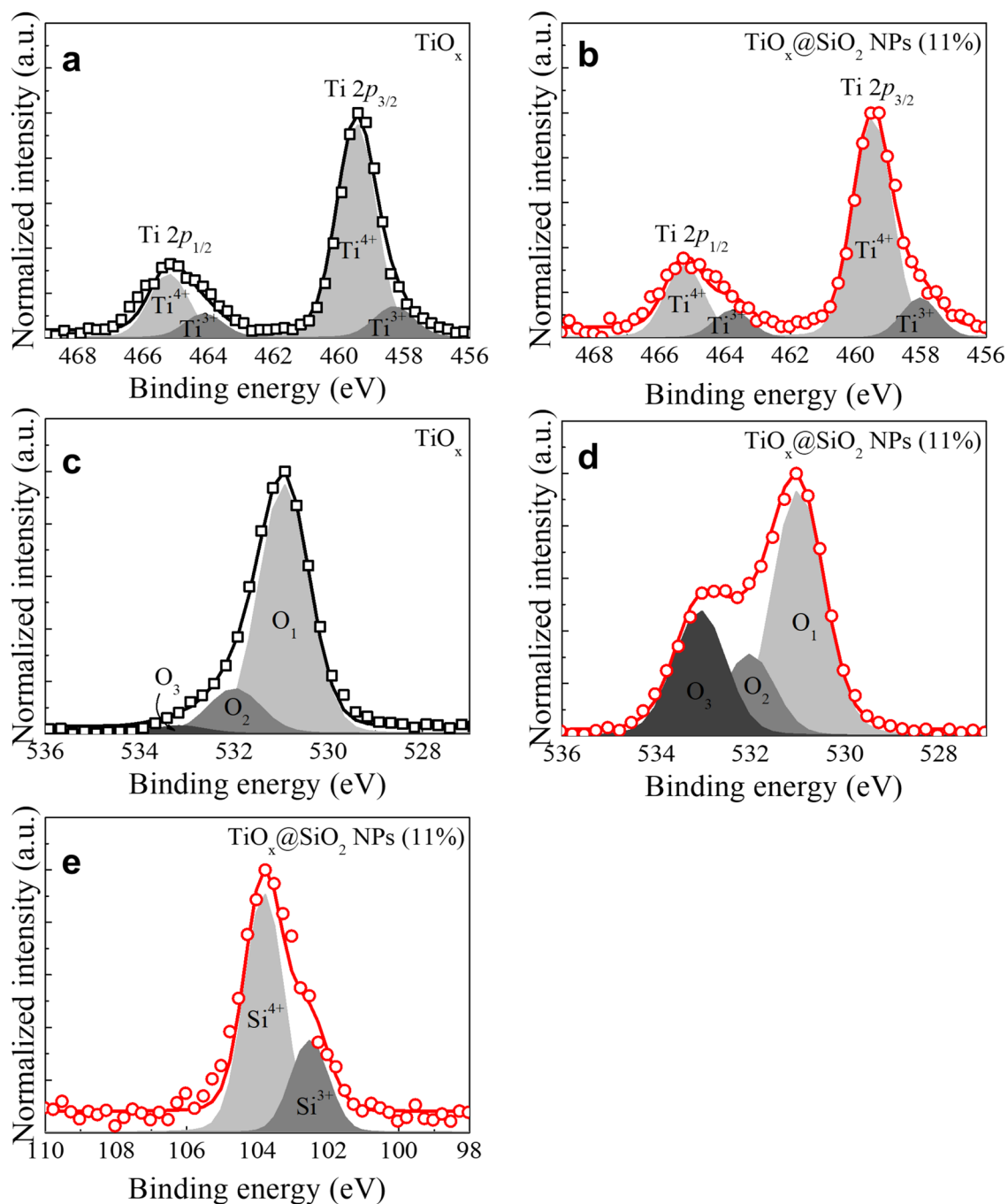
Figure 4. XPS core-level spectra of (**a**,**b**) Ti 2p, (**c**) and (**d**) O 1s for TiO$_x$ and TiO$_x$@SiO$_2$ NPs films, and (**e**) Si 2p for TiO$_x$@SiO$_2$ NPs film.

shown in Fig. 6a. The I–V curve consists of three regions with slopes of (1.06, 1.79, and 2.41), which respectively relate to the Ohmic region ($I \propto V$) dominated by thermally generated free carriers; the Child's law region ($I \propto V^2$), in which traps are filled by electrons; and the steep increase region ($V \propto I^n$, $n > 2$)[29,41–43]. In the TiO$_x$-based switching device, oxygen vacancies in the TiO$_x$ matrix serve as electron traps, and they lead to the formation or rupture of the conductive path. Therefore, the migration of oxygen vacancies is an important role in the deviation of slopes. In the high-voltage region, all traps in the TiO$_x$ matrix are filled by electrons, then electrons flow through the conduction band of TiO$_x$, after which the TiO$_x$ device achieves the SET process. For the RESET process, the slope is closer to ~1.00, which is attributed to the Ohmic behavior being the dominant carrier transport mechanism during the RESET process. Both the Ohmic and SCLC mechanisms are associated with the bulk controlled mechanism, meaning that the TiO$_x$ device is properly explained by the conductive filament model. In the case of the TiO$_x$@SiO$_2$ NPs device, it is important to understand the conduction mechanism of each RS. Figure 6b shows the log I – log V plotting result of the TiO$_x$@SiO$_2$ NPs device, and the carrier transport mechanism of LRS
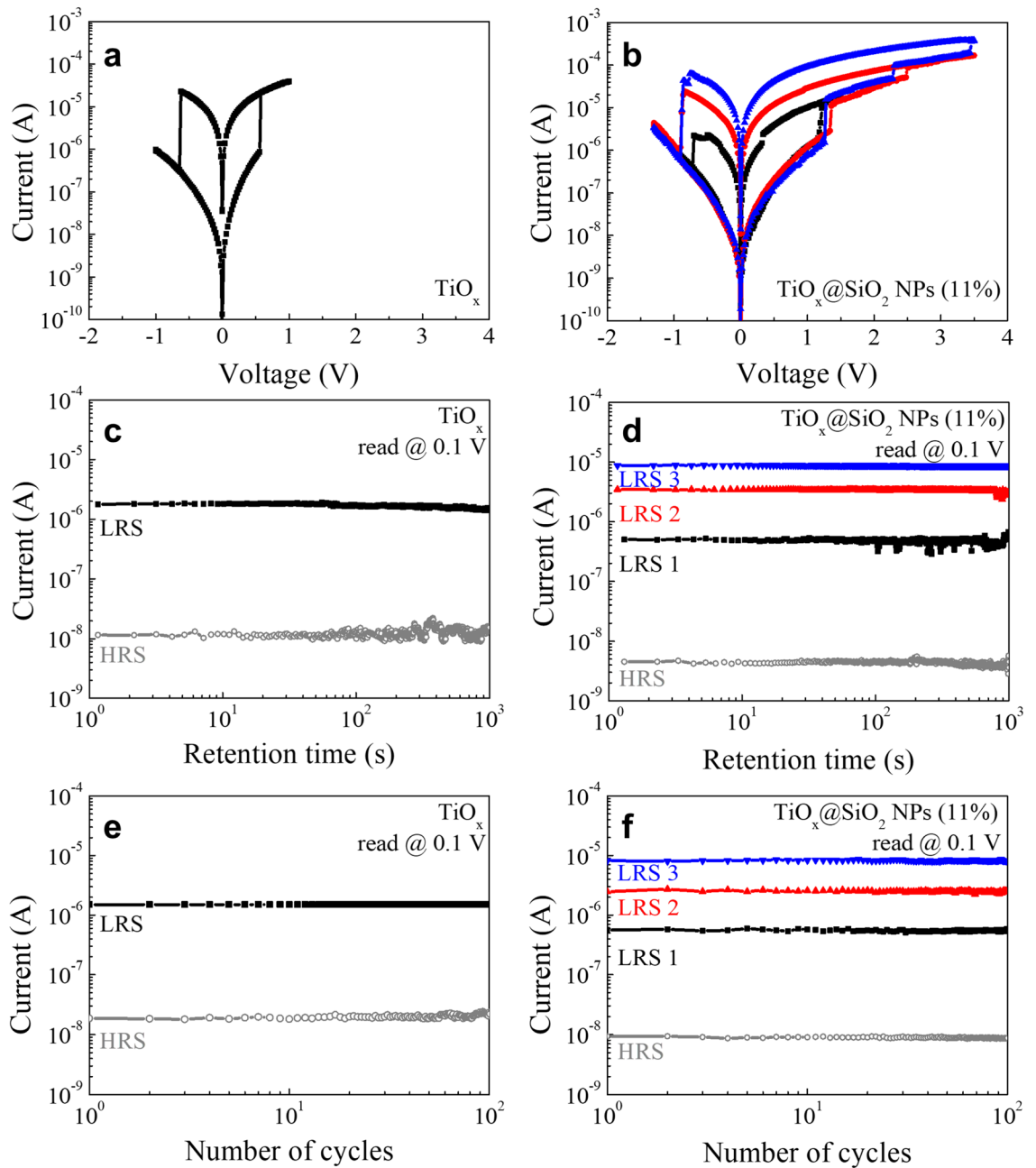
Figure 5. (**a,b**) Resistive switching curves, (**c,d**) retention performance, and (**e,f**) endurance performance of the TiO$_x$ and TiO$_x$@SiO$_2$ NPs switching devise.

1 also corresponds to a trap-controlled SCLC in the range from 0 to 1.28 V[44]. Upon further increasing the voltage above 1.28 V, the trap-controlled SCLC is not explained, due to the decreases in the fitted lines to 1.82 and 1.58. To validate the transport characteristics of the LRS 2 and LRS 3, we apply the trap-assisted tunnelling (TAT) model and Poole–Frenkel (P–F) emission, as shown in Fig. 6c,d, respectively. These conduction mechanisms are typically calculated when examining oxide materials with a high concentration of traps. The I–V curve is linearly fitted by the TAT model, which describes a plot of ln (I) − 1/V, as shown in Fig. 6c. The TAT is attributed to the traps, such as oxygen vacancies, which help the electrons tunnel from cathode to anode[45]. In the high-voltage region, the discrete trap sites are created in the switching stack, and carrier conduction becomes possible through the trap-to-trap tunnelling process. Moreover, the P–F emission with a plot of ln (I/V) − V$^{1/2}$ displays a linear relationship in the high-voltage region, as shown in Fig. 6d. The P–F emission results indicate that the carriers trapped in trap sites obtain enough energy, such as a high electric field or high temperature, that the trapped carriers are excited from the energy barriers of the traps to the conduction band[29]. It is known that the transition of P–F emission, which is typically at high-voltage, is much higher because of the much closer spacing of the traps. Therefore, the electron occupation probability of the nearest traps is very low, since all the electrons are quickly swept out through P–F emission[46]. In our case, multiple RSs can be attributed to various conduction
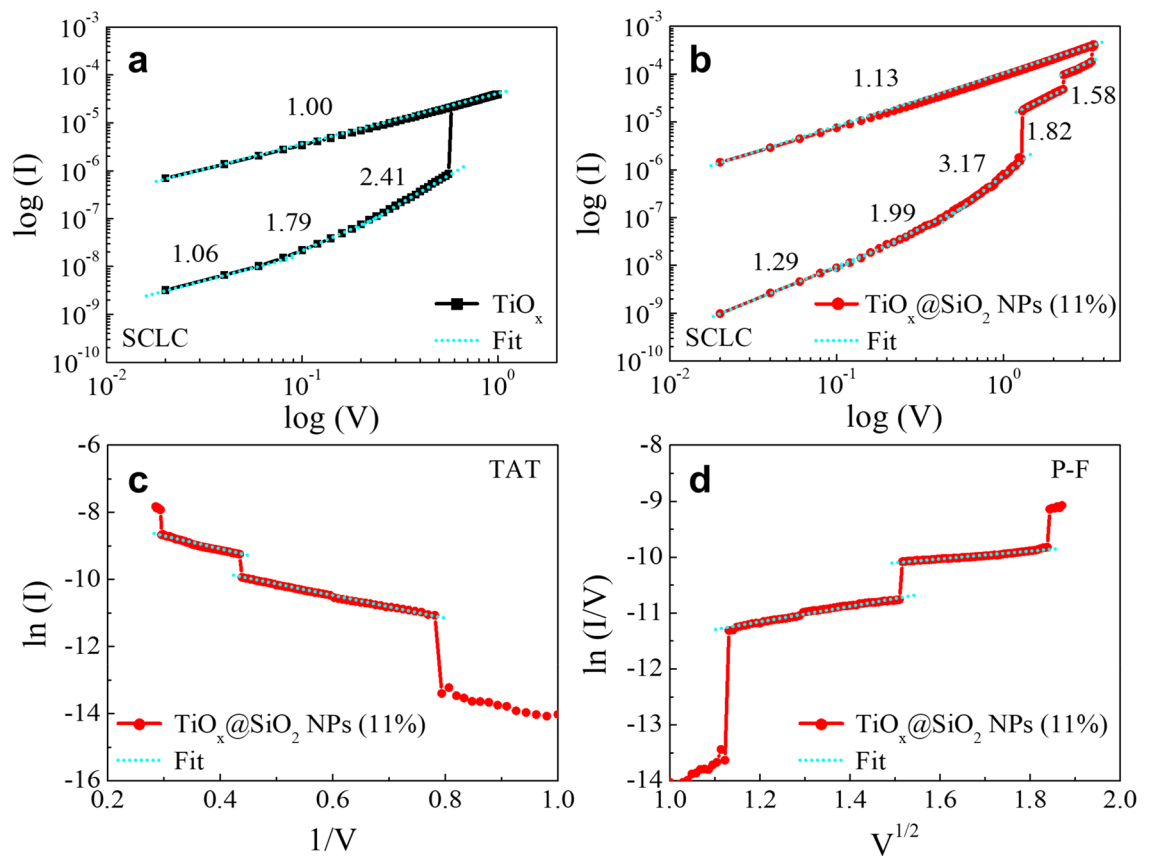
Figure 6. Log I–log V plot of I–V curves of the (**a**) TiO$_x$ and (**b**) the TiO$_x$@SiO$_2$ NPs switching devices. The TiO$_x$@SiO$_2$ NPs implies (**c**) trap-assisted tunneling, and (**d**) Poole–Frenkel emission in the high-voltage region.

mechanisms, including the TAT model and P–F emission under a high electric field. Based on these analyses, we can understand the electron conduction mechanism in each RS. The conduction mechanism for LRS can also be explained by Ohmic conduction: In the low-voltage region, lots of traps in the TiO$_x$ matrix and SiO$_2$ NPs connect with each other, and this contributes to Ohmic conduction. Upon increasing the voltage, the conductive path into the TiO$_x$ matrix and SiO$_2$ NPs begins to be formed. When large current flows through the conductive path, the conduction mechanism in LRS is explained by Ohmic behavior with a slope of 1.13, as shown in Fig. 6b.

Figure 7a–e show schematics of the energy band diagrams of the TiO$_x$ and TiO$_x$@SiO$_2$ NPs devices, respectively, in the initial and SET states. As shown in Fig. 7b, with the application of positive voltages to TE, the traps below the TiO$_x$ conduction band are gradually filled with electrons. After all of the traps are filled (i.e., after exceeding the trap-filled limit voltage, V_{TFL}), the current rapidly increases, and the TiO$_x$ device switches from HRS to LRS. When negative voltage is applied to the TE, de-trapping of the oxygen vacancies occurs, and the TiO$_x$ device transitions from LRS to HRS. The dominant mechanism in the TiO$_x$@SiO$_2$ NPs device is almost the same as that in the TiO$_x$ device. In the initial state of the TiO$_x$@SiO$_2$ NPs device, the energy barrier exists at TiO$_x$/SiO$_2$ NPs, as shown in Fig. 7c. Therefore, compared to the TiO$_x$ device, more sufficient voltage is needed to pass across TiO$_x$ and SiO$_2$ NPs. Upon applying voltages to the TiO$_x$@SiO$_2$ NPs device, the electrons can migrate from TiO$_x$ to SiO$_2$ NPs, and thus overcome the energy barrier of TiO$_x$/SiO$_2$ NPs. The electrons move along the tilted conduction band of the TiO$_x$ layer, and then the TiO$_x$ device reaches LRS (LRS 1). When the higher voltage is applied to the TiO$_x$ device, the trapped electrons could either hop to other trap sites or be excited to the conduction band. As a result, the current level abruptly increases, and the TiO$_x$ device eventually reaches higher current levels (LRS 2 and LRS 3). When the negative voltage is applied to the electrode, the conductive filament ruptures, and the device switches from LRS to HRS.

Conclusion

In conclusion, we have demonstrated an improvement in the optical and electrical characteristics of a TiO$_x$ resistive switching device with the embedment of SiO$_2$ NPs, which are structured with ITO/TiO$_x$@SiO$_2$ NPs/ITO on glass substrate. The TiO$_x$@SiO$_2$ NPs device structure shows a high transmittance over 95% in the visible range. The embedment of SiO$_2$ NPs into the TiO$_x$ matrix induces higher oxygen vacancies in the TiO$_x$ matrix; further, because Si–O has a higher bond dissociation energy than Ti–O, it determines the formation and rupture of the conductive path through the application of an electric field. The TiO$_x$@SiO$_2$ NPs device exhibits stable bipolar resistive switching characteristics, and a distinguishable multi-level of four states (three of LRS and one of HRS) can be obtained by applying voltage. Moreover, the device shows a long retention time for 10^3 s as well as good
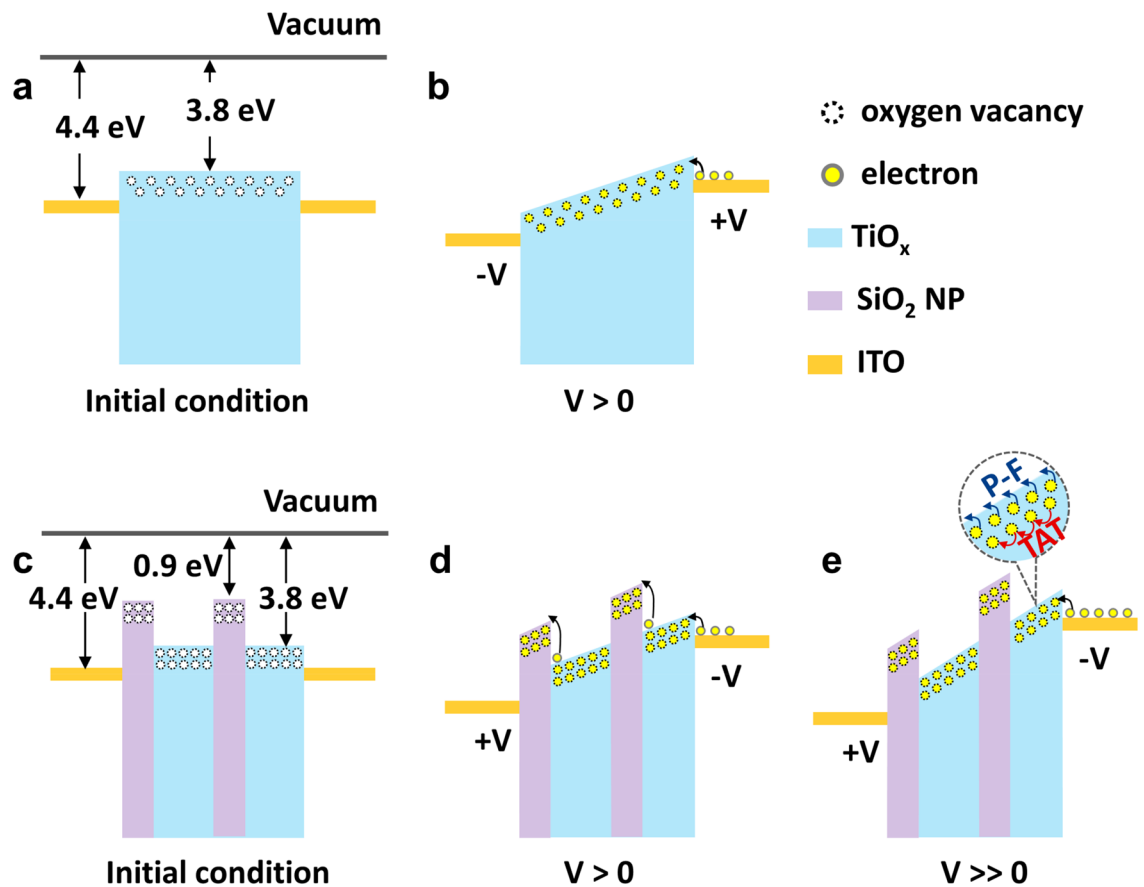
Figure 7. Schematic energy band diagrams for (**a,b**) the TiO$_x$ device and (**c–e**) the TiO$_x$@SiO$_2$ NPs under initial states and SET process.

endurance for 10^2 cycles. The dominant switching mechanism is based on the conductive filament model, which includes the trap-controlled SCLC. After all the traps are filled out, the TAT and P–F emission gradually become dominant in the high-voltage region. The embedment of SiO$_2$ NPs in the TiO$_x$-based device can lead to improved electrical characteristics, such as multi-level switching, as well as low-voltage operation with stable resistive states, thus making it a promising method for future non-volatile memory devices.

Methods

Synthesis and fabrication.   TiO$_x$ was synthesized using the sol–gel method, which is based on the hydrolysis of alkoxides in alcoholic solutions in the presence of an acid catalyst. Titanium isopropoxide (TTIP, Ti[OCH(CH3)2]4, Aldrich Chemical Co., 97%), ethanol (C$_2$H$_5$OH, Daejung 99.9%), and nitric acid (HNO$_3$, Merck, 70%) were used as the starting materials, and distilled (DI) water was used for hydrolysis. The molar ratio of the starting solution was 1 of TTIP, 1 of DI water, 25 of ethanol, and 0.2 of nitric acid[47]. The solution of nitric acid, DI water, and half ethanol was added dropwise to the solution of TTIP and ethanol at 0 °C under continuous vigorous stirring. The transparent solution finally resulted, and it was diluted using ethanol with a ratio of 1:1.

Fabrication of switching device.   To fabricate the TiO$_x$-based switching memory device with a cross-bar array architecture, a glass substrate was first cleaned by wet cleaning through ultra-sonication for 10 min each in acetone, isopropyl alcohol, and DI water, before being dried in an oven at 80 °C for 20 min. Next, the promoter was coated on the glass substrate at 1000 rpm for 10 s and 5000 rpm for 60 s to enhance the adhesion of the photoresist, after which negative photoresist (5214) was coated at the same condition, followed by soft baking at 110 °C for 140 s. Then, the glass substrate was exposed to UV light for 3 s with photomask using an aligner. After being baked again at 120 °C for 200 s, the glass substrate was exposed again to UV light for 7 s without photomask, after which it was soaked in developer for 60 s. Subsequently, ITO layer was deposited on the patterned photoresist using direct current sputtering, and the substrate was soaked in acetone for lift-off of the photoresist, leading to the BE patterns. In the next step, 50 nm-thick TiO$_x$ film was coated on the patterned BE of ITO by the spin coating method at 5500 rpm for 60 s. For the one-step solution process, 230 μL of SiO$_2$ NPs (Nanocomposix, 20 ± 4 nm) and 100 μL of diluted TiO$_x$ solution were mixed together under continuous stirring for 15 min, after which the mixed solution was coated with the same condition. Next, the coated TiO$_x$ and SiO$_2$ NPs-embedded

TiO$_x$ (TiO$_x$@SiO$_2$ NPs) were dried at 80 °C for 20 min in an oven. All of the TiO$_x$ and TiO$_x$@SiO$_2$ NPs films had an amorphous structure (Fig. S5). Then, to obtain the TE pattern, the same process used for photoresist patterning and ITO deposition was performed repeatedly on the TiO$_x$ and TiO$_x$@SiO$_2$ NPs layers. Finally, the cross-bar array ReRAM structures with an active device area of 100 μm^2 were obtained.

Characterization. The structural characteristics were observed using atomic force microscopy (AFM, Bruker Corp. N8 NEOS) measurement. The scanning was performed using non-contact mode and a scan size of 5×5 um^2. The cross-sectional specimens were prepared using a focused ion beam (FIB, FEI Helios 650) system, then examined using field effect transmission electron microscopy (TEM, JEOL Ltd. JEM-F200) with energy-dispersive spectroscopy (EDS). The optical transmittance was measured with ultraviolet–visible (UV–Vis, TEC5 MultiSpec) spectroscopy in the range from 400 to 800 nm. The thickness and optical constant of the TiO$_x$ and TiO$_x$@SiO$_2$ NPs layers were examined through spectroscopic ellipsometry (SE, J. A. Woollam-VASE) measurement from 1 to 5 eV with an incident angle of 65°. To accurately investigate the composition and chemical state of TiO$_x$ and TiO$_x$@SiO$_2$ NPs, x-ray photoelectron spectroscopy (XPS, ESCA Veresprobe II) was conducted using a monochromatic Al Kα source (hv = 1486.7 eV) with a pass energy of 29.5 eV. The current–voltage (I–V) was measured using a semiconductor analyzer (Keithley-4200). During the I–V measurement, the bias was applied to the TE of ITO, and the BE of ITO was grounded under ambient conditions.

References

1. Waser, R., Dittmann, R., Staikov, G. & Szot, K. Redox-based resistive switching memories—Nanoionic mechanisms, prospects, and challenges. *Adv. Mater.* **21**, 2632–2663 (2009).
2. Antonio, C. T., John, P. S., Gilberto, M.-R. & Williams, R. S. Sub-nanosecond switching of a tantalum oxide memristor. *Nanotechnology* **22**, 485203 (2011).
3. Hermes, C. *et al.* Analysis of transient currents during ultrafast switching of TiO$_2$ nanocrossbar devices. *IEEE Electron Device Lett.* **32**(8), 1116–1118 (2011).
4. Bousoulas, P., Giannopoulos, I., Asenov, P., Karageorgiou, I. & Tsoukalas, D. Investigating the origins of high multilevel resistive switching in forming free Ti/TiO$_{2-x}$-based memory devices through experiments and simulations. *J. Appl. Phys.* **121**, 094501 (2017).
5. Son, J. Y. *et al.* A HfO$_2$ thin film resistive switch based on conducting atomic force microscopy. *Solid-State Lett.* **14**(8), H311–H313 (2011).
6. Strukov, D. B., Snider, G. S., Steward, D. R. & Williams, R. S. The missing memristor found. *Nature* **453**, 80–83 (2008).
7. Wedog, A. *et al.* Nanoscale cation motion in TaO$_x$, HfO$_2$, and TiO$_x$ memristive systems. *Nat. Nanotechnol.* **11**, 67–74 (2016).
8. Nardi, F. *et al.* Control of filament size and reduction of reset below 10 uA in NiO resistance switching memories. *Solid-State Electron.* **58**, 42–47 (2011).
9. Yang, J. J. *et al.* Memristive switching mechanism for metal/oxide/metal nanodevices. *Nat. Nanotechnol.* **3**, 429–433 (2008).
10. Rohde, C. *et al.* Identification of a determining parameter for resistive switching of TiO$_2$ thin films. *Appl. Phys. Lett.* **86**, 262907 (2005).
11. Jameson, J. R. *et al.* Field-programmable rectification in rutile TiO$_2$ crystals. *Appl. Phys. Lett.* **91**, 112101 (2007).
12. Zhou, G. *et al.* Coexistence of negative differential resistance and resistive switching memory at room temperature in TiO$_x$ modulated by moisture. *Adv. Electron. Mater.* **4**, 1700567 (2018).
13. Sung, C., Lim, S. & Hwang, H. Experimental determination of the tunable threshold voltage characteristics in a Ag$_x$Te$_{1-x}$/Al$_2$O$_3$/TiO$_2$-based hybrid memory device. *IEEE Electron Device Lett.* **41**(5), 713–716 (2020).
14. Nauenheim, C., Kuegeler, C., Ruediger, A. & Waser, R. Investigation of the electroforming process in resistively switching TiO$_2$ nanocrosspoint junctions. *Appl. Phys. Lett.* **96**, 122902 (2010).
15. Kim, S. *et al.* Flexible crossbar-structured resistive memory arrays on plastic substrates via inorganic-based laser lift-off. *Adv. Mater.* **26**, 7480–7487 (2014).
16. Zhao, L. *et al.* Multi-level control of conductive nano-filament evolution in HfO$_2$ ReRAM by pulse-train operation. *Nanoscale* **6**, 5698–5702 (2014).
17. Chae, S. C. *et al.* Multilevel unipolar resistance switching in TiO$_2$ thin films. *Appl. Phys. Lett.* **95**, 093508 (2009).
18. Carta, D. *et al.* X-ray absorption spectroscopy study of TiO$_{2-x}$ thin films for memory applications. *J. Phys. Chem. C* **119**, 4362–4370 (2015).
19. Lim, D.-H. *et al.* Electric field effect dominated bipolar resistive switching through interface control in a Pt/TiO$_2$/TiN structure. *RSC Adv.* **5**, 221–230 (2015).
20. Alexander, S. *et al.* Role of the electrode material on the RESET limitation in oxide ReRAM device. *Adv. Elecron. Mater.* **4**, 1700243 (2018).
21. Tsigkourakos, M., Bousoulas, P., Aslanidis, V., Skotadis, E. & Tsoukalas, D. Ultra-low power multilevel switching with enhanced uniformity in forming free TiO$_{2-x}$ based RRAM with embedded Pt nanocrystals. *Phys. Status Solidi A* **214**, 1700570 (2017).
22. Yoon, J. H. *et al.* Highly improved uniformity in the resistive switching parameters of TiO$_2$ thin films by inserting Ru nanodots. *Adv. Mater.* **25**(14), 1987–1992 (2013).
23. Kotaka, Y. Direct visualization method of the atomic structure of light and heavy atoms with double-detector C$_s$-corrected scanning transmission electron microscopy. *Appl. Phys. Lett.* **101**, 133107 (2012).
24. Lariviere, G. P., Frigerio, J. M., Bridou, F. & Rivory, J. Modelling of ellipsometric data of inhomogeneous TiO$_2$ films. *Thin Solid Films* **234**, 458–462 (1993).
25. Mohamed, S. H., Kappertz, O., Pedersen, T. P. L., Drese, R. & Wuttig, M. Properties of TiO$_x$ coatings prepared by dc magnetron sputtering. *Phys. Stat. Sol. A* **198**(1), 224–237 (2003).
26. Xian, S. *et al.* Effect of oxygen stoichiometry on the structure, optical and epsilon-near-zero properties of indium tin oxide films. *Opt. Express* **27**(20), 28618–28628 (2019).
27. Zhao, M.-J. *et al.* Suppression of oxygen vacancy defects in sALD-ZnO films annealed in different conditions. *Materials* **13**, 3910 (2020).
28. Khlebtsov, B. N., Khanadeev, V. A. & Khlebtsov, N. G. Determination of the size, concentration, and refractive index of silica nanoparticles from turbidity spectra. *Langmuir* **24**, 8964–8970 (2008).

29. Jung, S. *et al.* Resistive switching characteristics of solution-processed transparent TiO_x for nonvolatile memory application. *J. Electrochem. Soc.* **157**(11), H1042–H1045 (2010).
30. Xiao, M., Musselman, K. P., Duley, W. W. & Zhou, Y. N. Reliable and low-power multilevel resistive switching in TiO_2 nanorod arrays structured with a TiO_x seed layer. *ACS Appl. Mater. Interfaces* **9**, 4808–4817 (2017).
31. Li, W., Liang, R., Hu, A., Huang, Z. & Zhou, Y. N. Generation of oxygen vacancies in visible light activated one-dimensional iodine TiO_2 photocatalysts. *RSC Adv.* **4**(70), 36959–36966 (2014).
32. Kim, A., Song, K., Kim, Y. & Moon, J. All solution-processed, fully transparent resistive memory devices. *ACS Appl. Mater. Interfaces* **3**, 4525–4530 (2011).
33. Regoutz, A. *et al.* Role and optimization of active oxide layer in TiO_2-based RRAM. *Adv. Funct. Mater.* **26**, 507–513 (2016).
34. Jiang, H. *et al.* Bias-polarity-dependent resistance switching in $W/SiO_2/Pt$ and $W/SiO_2/Si/Pt$ structures. *Sci. Rep.* **6**, 22216 (2016).
35. Luo, Y.-R. *Comprehensive Handbook of Chemical Bond Energies* (CRC Press, 2007).
36. Kwon, D.-H. *et al.* Atomic structure of conducting nanofilaments in TiO_2 resistive switching memory. *Nat. Nanotechnol.* **5**, 148–153 (2010).
37. Kamiya, K. *et al.* ON-OFF switching mechanism of resistive-random-access-memories based on the formation and disruption of oxygen vacancy conducting channels. *Appl. Phys. Lett.* **100**, 073502 (2012).
38. Park, J. *et al.* Multibit operation of TiO_x-based ReRAM by Schottky barrier height engineering. *IEEE Electron Device Lett.* **32**(4), 476–478 (2011).
39. Zhang, H. *et al.* Understanding the coexistence of two bipolar resistive switching modes with opposite polarity in $Pt/TiO2/Ti/Pt$ nanosized ReRAM devices. *ACS Appl. Mater. Interfaces* **10**, 29766–29778 (2018).
40. Shao, X. L. *et al.* Electronic resistance switching in the $Al/TiO_x/Al$ structure for forming-free and area-scalable memory. *Nanoscale* **7**, 11063–11074 (2015).
41. Barman, A. *et al.* Resistive switching behavior in oxygen ion irradiated TiO_{2-x} films. *J. Phys. D Appl. Phys.* **51**, 065306 (2018).
42. Zheng, P. *et al.* Photo-induced negative differential resistance in a resistive switching memory device based on $BiFeO_3/ZnO$ heterojunctions. *Appl. Mater. Today* **14**, 21–28 (2019).
43. Zhou, G., Yang, X., Xiao, L., Sun, B. & Zhou, A. Investigation of a submerging redox behavior in Fe_2O_3 solid electrolyte for resistive switching memory. *Appl. Phys. Lett.* **114**, 163506 (2019).
44. Jeong, H. Y., Lee, J. Y., Ryu, M.-K. & Choi, S.-Y. Bipolar resistive switching in amorphous titanium oxide thin film. *Phys. Status Solidi RRL* **4**(1–2), 28–30 (2010).
45. Lim, E. W. & Ismail, R. Conduction mechanism of valence change resistive switching memory: A survey. *Electronics* **4**(3), 586–613 (2015).
46. Yu, S., Guan, X. & Wong, H.-S.P. Conduction mechanism of $TiN/HfO_x/Pt$ resistive switching memory: A trap-assisted-tunneling model. *Appl. Phys. Lett.* **99**, 0635 (2011).
47. Lin, H., Kozuka, H. & Yoko, T. Preparation of TiO_2 films on self-assembled monolayers by sol-gel method. *Thin Solid Films* **315**, 111–117 (1998).

Acknowledgements

Author contributions

S.K. and K.-B.C. conceived the idea and designed the experiments. S.K. conducted the experiments and evaluated the data with help of M.-J. K..S.K. and K.-B.C. wrote the manuscript. All authors read and approved the manuscript for submission.

Competing interests

The authors declare no competing interests.

Additional information

Supplementary Information The online version contains supplementary material available at https://doi.org/10.1038/s41598-021-89315-z.

Correspondence and requests for materials should be addressed to K.-B.C.

Reprints and permissions information is available at www.nature.com/reprints.

Publisher's note Springer Nature remains neutral with regard to jurisdictional claims in published maps and institutional affiliations.